

# Negative-mass exciton polaritons induced by dissipative light-matter coupling in an atomically thin semiconductor

M. Wurdack,<sup>1,\*</sup> T. Yun,<sup>1,2</sup> M. Katzer,<sup>3</sup> A. G. Truscott,<sup>4</sup>  
 A. Knorr,<sup>3</sup> M. Selig,<sup>3</sup> E. A. Ostrovskaya,<sup>1,†</sup> and E. Estrecho<sup>1,‡</sup>  
<sup>1</sup>*ARC Centre of Excellence in Future Low-Energy Electronics Technologies and  
 Department of Quantum Science and Technology, Research School of Physics,  
 The Australian National University, Canberra, ACT 2601, Australia*  
<sup>2</sup>*Department of Materials Science and Engineering,  
 Monash University, Clayton, Victoria, 3800, Australia*  
<sup>3</sup>*Nichtlineare Optik und Quantenelektronik, Institut für Theoretische Physik,  
 Technische Universität Berlin, 10623 Berlin, Germany*  
<sup>4</sup>*Department of Quantum Science and Technology, Research School of Physics,  
 The Australian National University, Canberra, ACT 2601, Australia*

Dispersion engineering is a powerful and versatile tool that can vary the speed of light signals [1] and induce negative-mass effects in the dynamics of electrons [2], quasiparticles, [3] and quantum fluids [4, 5]. Here, we show that dissipative coupling of bound electron-hole pairs (excitons) and photons in an optical microcavity [6] can lead to the formation of exciton polaritons with an inverted dispersion of the lower polariton branch and hence, a negative mass. We perform a direct measurement of the anomalous dispersion in an atomically thin WS<sub>2</sub> crystal [7] embedded in a planar microcavity and demonstrate that the propagation direction of the negative-mass polaritons is opposite to their momentum. Our study introduces a new concept of non-Hermitian dispersion engineering for exciton polaritons and opens a pathway for realising new phases of quantum matter in a solid state.

Losses are ubiquitous in nature and are usually perceived as detrimental to the performance of electronic and photonic devices. However, recent understanding of the physics of non-Hermitian systems with loss and gain has led to the possibility of novel properties and functionalities by judicious control of losses. This concept is most powerfully demonstrated in non-Hermitian photonics [8–10], where non-Hermitian spectral degeneracies (exceptional points) and associated symmetry-breaking transitions fundamentally change the laws of wave propagation and scattering. Although the study of non-Hermitian physics in quantum electronic systems remains difficult, significant progress has been achieved in hybrid photonic systems, where photons are strongly coupled to electronic excitations in a solid state to form exciton polaritons, part-light part-matter hybrid quasiparticles [6]. Nontrivial topology of the eigenstates [11, 12] and mode selectivity [13] in the vicinity of the exceptional points, band engineering [14] and nonlinear localisation [15] in non-Hermitian lattices, emergence of non-Hermitian topology [16] and divergent quantum geometric metric near an ex-

ceptional point [17] have been demonstrated in the strong light-matter coupling regime.

Here, we dramatically modify the exciton-polariton dispersion by exploiting a previously undetected non-Hermitian component of exciton-photon interaction called dissipative coupling [18]. Our microscopic theory shows that this type of coupling can arise from the interplay of exciton-phonon scattering and photon losses. Also known as external coupling via the continuum [19], dissipative coupling leads to level attraction or clustering [19, 20] and resonance trapping [21] in other physical systems. This is in contrast to the well known coherent (or internal) coupling which always leads to level repulsion. We show theoretically that the interplay between the coherent and dissipative light-matter coupling results in an inverted dispersion of exciton polaritons in a planar microcavity. We directly measure this anomalous dispersion and demonstrate the negative-mass transport of exciton polaritons in monolayer WS<sub>2</sub> embedded in an optical microcavity formed by two distributed Bragg reflector (DBR) mirrors with a polymer spacer [22] at room temperature.

To demonstrate the principle of non-Hermitian dispersion engineering, we start with an effective Hamiltonian given by  $H = H_0 - iWW^\dagger$  [21] describing the coherent (internal) and dissipative (external) coupling of cavity photons  $|C\rangle$  and excitons  $|X\rangle$ :

$$H = \begin{pmatrix} E_c & V \\ V & E_x \end{pmatrix} - i \begin{pmatrix} \sqrt{\gamma_c} & \sqrt{g} \\ 0 & \sqrt{\gamma_x} \end{pmatrix} \begin{pmatrix} \sqrt{\gamma_c} & 0 \\ \sqrt{g} & \sqrt{\gamma_x} \end{pmatrix}. \quad (1)$$

Here, the Hermitian term  $H_0$  models the coherent coupling of excitons and photons with the bare energies  $E_{c,x}$ , respectively. The coupling strength  $V$  is proportional to the exciton oscillator strength and the overlap of the exciton dipole with the confined electric field of the cavity photon [6]. The matrix  $W$  describes the external coupling to two decay channels [21]:  $\gamma_c$  is the coupling of cavity photons to the continuum of states outside the cavity due to the imperfect mirrors limiting their lifetimes,  $\gamma_x$  is the coupling to radiative and non-radiative

channels, resulting in the homogeneous linewidth broadening of excitons [23, 24], and  $g$  captures the coupling of cavity photons and excitons to the same non-radiative decay channel.

The dissipative coupling parameter  $g$  controls the imaginary part of the exciton-photon coupling, which results in a level attraction. To elucidate its origin, we study the interaction between excitons, phonons, cavity photons, and the photon bath outside the cavity using a microscopic theory (see Supplementary Information). The self-consistent calculations show that the interplay between exciton-phonon scattering and cavity photon losses leads to dissipative coupling, which is prominent in monolayer transition metal dichalcogenides (TMDCs) where the exciton-phonon scattering plays a significant role [23–26]. We note that various types of dissipative coupling of different origins have been observed in optomechanical [18] and magnon-photon systems [20], and open microwave cavities [19, 21]. It also appears in theoretical studies of fragmented exciton-polariton condensates [27] and excitons polaritons coupled to an optomechanical resonator [28].

The exciton-photon coupling in Eq. 1 gives rise to the complex upper ( $U$ ) and lower ( $L$ ) eigenvalue branches:

$$E_{U,L} - i\gamma_{U,L} = \langle \tilde{E} \rangle \pm \frac{1}{2} \sqrt{(\Delta - i\delta)^2 + 4(V - i\sqrt{g\gamma_x})^2}, \quad (2)$$

where  $\langle \tilde{E} \rangle = \langle E \rangle - i\langle \gamma \rangle$  is the mean complex eigenvalue with  $\langle \gamma \rangle = (\gamma_c + g + \gamma_x)/2$ ,  $\Delta = E_c - E_x$  is the bare energy difference and  $\delta = \gamma_c + g - \gamma_x$ . The eigenvalues and eigenvectors will simultaneously coalesce at the exceptional point when  $V = |\delta|/2$  and  $\Delta = 2\sqrt{g\gamma_x}$ . Note that when  $g = 0$ , the non-Hermitian term  $-iWW^\dagger$  simply describes the decay rates  $\gamma_{c,x}/\hbar$  of the bare (uncoupled) cavity photon and exciton, respectively.

The level and linewidth dynamics for different strengths of  $V$  and  $g$  are shown in Fig. 1a,b. We focus on the strong coupling regime at  $V > |\delta|/2$  characterised by energy anticrossings and linewidth crossings. In this regime, the eigenstates correspond to the hybrid exciton-polariton quasiparticles [6, 29–31]. The corresponding shifts of the polariton energies from the bare exciton and photon energies, defined as  $\Delta_{UL} = \Re(E_U - E_L) - \Delta$ , is plotted in Fig. 1c as a function of  $\Delta$ . In the purely coherent coupling regime ( $g = 0$ ), the energies exhibit level repulsion (positive  $\Delta_{UL}$ ) with a maximum value at resonance ( $\Delta = 0$ ) where the linewidths cross. The level repulsion decreases monotonically with  $|\Delta|$ , reminiscent of the familiar Hermitian limit,  $\gamma_{c,x}, g \rightarrow 0$  [6].

The behaviour of the energy levels and linewidths is drastically modified when the dissipative coupling  $g$  is introduced. The linewidth crossing shifts towards higher  $\Delta$  leaving a linewidth repulsion close to resonance, which leads to the so-called resonance trapping of the long-lived state [21]. Remarkably, the energy shift  $\Delta_{UL}$  becomes negative for a wide range of  $\Delta$ , indicating level attrac-

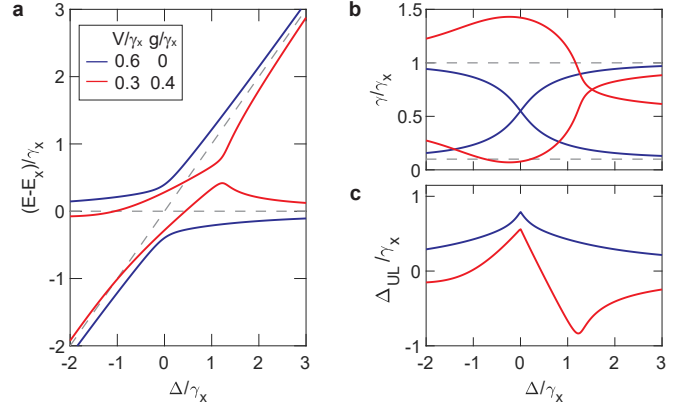


FIG. 1. **Coherent and dissipative coupling.** **a**, Energy and **b**, linewidth dynamics for different values of coherent  $V$  and dissipative  $g$  coupling strengths (in units of  $\gamma_x$ ). Dashed lines are the bare energy eigenvalues  $E_{c,x} - i\gamma_{c,x}$ . **c**, Energy shift  $\Delta_{UL}$  (see text) for the parameters used in **a** and **b**. In all cases, we tuned the cavity energy  $E_c$  while fixing  $E_x$  and  $\gamma_c = 0.1\gamma_x$ .

tion, which dominates at a positive exciton-photon detuning around  $\Delta \approx 2\sqrt{g\gamma_x}$ . This strongly  $\Delta$ -dependent energy shift is responsible for the anomalous dispersion of exciton polaritons presented in this work.

To describe the exciton-photon dispersion, we approximate the cavity photon dispersion as [6]  $E_c(k) = E_c + \hbar^2 k^2 / 2m_c$ , where  $E_0$  is the cavity resonance energy at normal incidence,  $\hbar k$  is the momentum along the plane of the cavity, and  $m_c$  is the in-plane effective mass of the cavity photon. The exciton energy  $E_x$  is approximately constant within the relevant momentum range probed here. Typical dispersion curves at a positive exciton-photon detuning,  $\Delta_0 = E_0 - E_x$ , are presented in Fig. 2a. Without the dissipative coupling ( $g = 0$ ), the dispersion features repelling branches corresponding to the well-known upper and lower exciton polaritons [6], where the lower branch is always redshifted from the exciton line. With increasing dissipative coupling strength  $g$ , level attraction starts to dominate, firstly starting at higher  $k$ . When  $g$  is large enough compared to  $V$ , the entire lower polariton branch is blueshifted from the exciton line. Note that the strongest level attraction occurs at a finite  $k$  for this set of parameters, resulting in two inversion peaks for the lower branch, reminiscent to the minimum of  $\Delta_{UL}$  in Fig. 1c.

To characterise the dispersion, we define the mass parameters [32]  $m_1(k) = \hbar^2 k [\partial_k E(k)]^{-1}$ , which determines the group velocity  $v_g = \hbar k / m_1$ , and  $m_2(k) = \hbar^2 [\partial_k^2 E(k)]^{-1}$ , which determines the acceleration due to an external field. Note that  $m_1$  is only negative around the inverted dispersion whereas  $m_2$  switches signs at the inflection points. The masses are plotted in Fig. 2b for the lower branches in Fig. 2a (indicated by arrows) with and without dissipative coupling. When  $g = 0$ ,  $m_1$  is

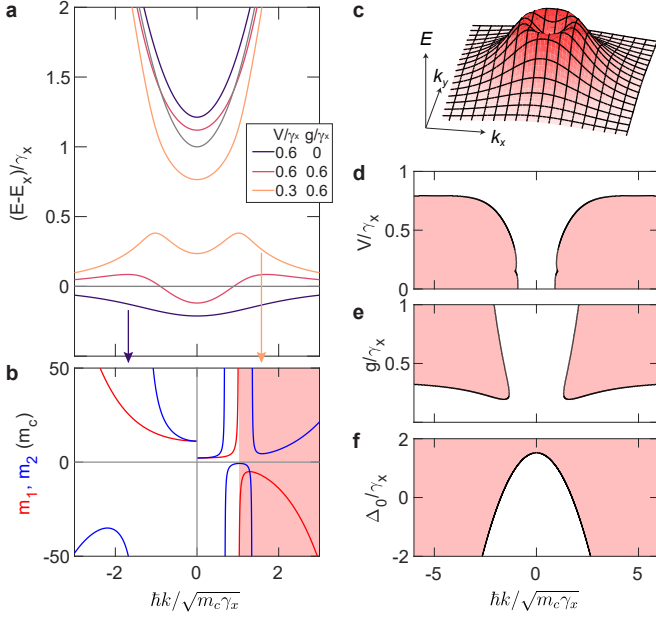


FIG. 2. **Anomalous dispersion of exciton polaritons.** **a**, Dispersion for different values of coherent and dissipative coupling strengths at fixed exciton–photon detuning  $\Delta_0 = \gamma_x$ . Thin grey lines are the bare exciton  $E_x$  and cavity photon  $E_c$  dispersions. **b**,  $k$ -dependent mass parameters  $m_1$  (red) and  $m_2$  (blue) corresponding to the two dispersions in **a** (see arrows). **c**, Lower polariton dispersion in two-dimensional  $k$ -space corresponding to **a** with  $V = 0.3\gamma_x$  and  $g = 0.6\gamma_x$ . **d-f**, Negative-mass ( $m_1 < 0$ ) regions (shaded) in  $k$ -space as a function of (d)  $V$  for  $g = 0.6\gamma_x$ ,  $\Delta_0 = \gamma_x$ , (e)  $g$  for  $V = 0.6\gamma_x$ ,  $\Delta_0 = \gamma_x$ , and (f)  $\Delta_0$  for  $V = 0.3\gamma_x$ ,  $g = 0.6\gamma_x$ .

positive for all momenta and  $m_2$  is only negative at finite  $k$ , a known feature of exciton polaritons [32]. This is in stark contrast to the case with  $g \neq 0$ , where both masses become negative near the inversion peak. While  $m_2$  switches back to positive sign,  $m_1$  remains negative for the plotted range of momenta, shown by the shaded region in Fig. 2b. Note that the sign of the  $m_1$  and  $m_2$  for the upper branch is largely unaffected by  $g$ .

It is important to point out that the inverted dispersion is isotropic, forming a ring in  $k$ -space, as shown in Fig. 2c. This is distinct from the inverted bands in periodic band structures, where the inversion peaks are localised at high-symmetry points only [5].

We further analyse the  $\Delta_0$ - $V$ - $g$  parameter space as a function of  $\hbar k$  to determine under which conditions the inverted dispersion appears. As expected, the negative-mass regions disappear when coherent coupling significantly dominates over dissipative coupling, as shown by the plots in Fig. 2d,e. Hence, either  $V$  has to be decreased or  $g$  increased to observe the inverted dispersion. The negative-mass regime also persists for a wide range of the exciton–photon detuning  $\Delta_0$ , as shown in Fig. 2f. However, the momentum range corresponding to the negative mass increases with the detuning  $\Delta_0$  and

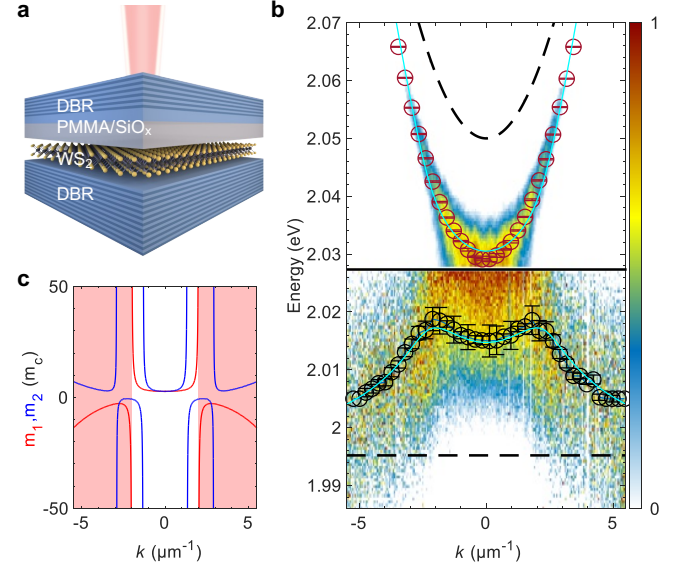


FIG. 3. **Experimental realisation of negative mass.** **a**, Schematics of the fabricated microcavity with embedded monolayer WS<sub>2</sub>. **b**, Momentum resolved PL spectrum at the position of the monolayer. The spectrum for  $E < 2.028$  eV is normalised at each  $k$  to visualise the shape of the lower branch. The black (red) circles are the fitted peak-positions of the lower (upper) branch. The solid cyan lines are the fitted energies of the upper and lower polaritons and the black dashed lines are the bare microcavity photons and excitons. **c**, Mass parameters (red)  $m_1$  and (blue)  $m_2$  for the lower branch in units of the fitted mass of the cavity photons, with the negative-mass regions shaded in red.

the dispersion becomes completely inverted at large positive  $\Delta_0/\gamma_x$ , a feature that was previously observed for trion polaritons [33] but due to a different mechanism. In summary, positive exciton–photon detunings and weaker  $V$  relative to  $g$  favour the negative-mass regime in our system.

Therefore, to demonstrate the effects of the anomalous dispersion experimentally, we fabricated a planar microcavity with an integrated monolayer WS<sub>2</sub> at a positive exciton–photon detuning and with reduced coherent coupling strength  $V$ . We achieved this with substrate engineering and our recently developed technology for integrating monolayer WS<sub>2</sub> into PMMA/SiO<sub>x</sub> spaced planar microcavities [22] (see Supplementary Information).

Figure 3a illustrates the sample design. Here, the WS<sub>2</sub> monolayer is mechanically transferred onto the bottom DBR protected with polymethyl-methacrylate (PMMA) against further deposition of the thin SiO<sub>x</sub> spacer and the top DBR (see Methods). The thin SiO<sub>x</sub> spacer allows us to carefully adjust the exciton–photon detuning  $\Delta_0$  to a positive value.

The momentum-resolved photoluminescence (PL) spectra of the polariton emission in this sample at room temperature (see Methods) are shown in Fig. 3b together

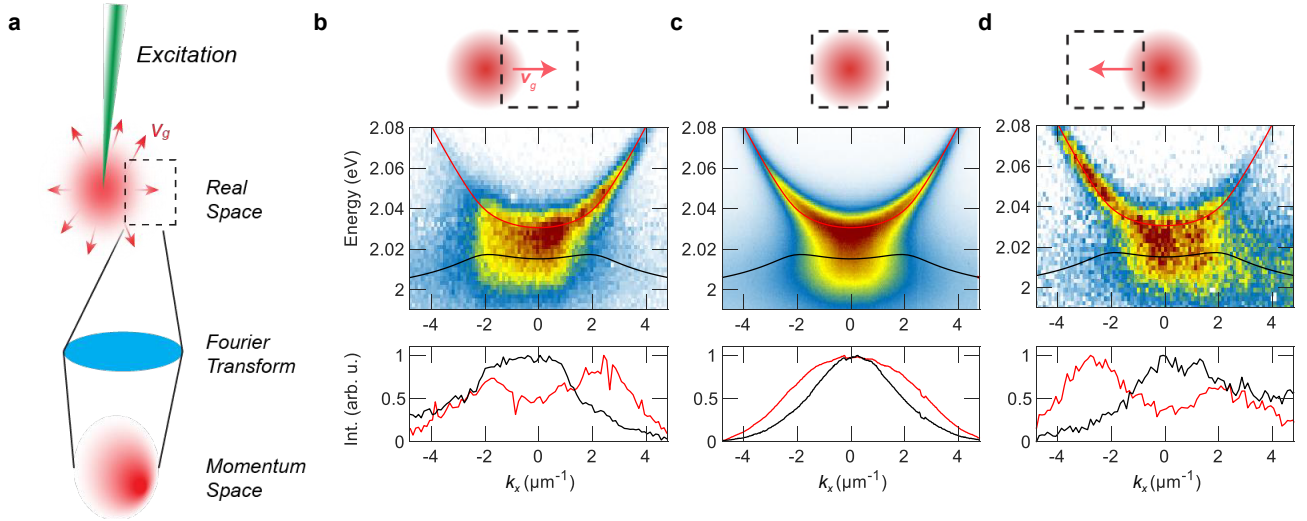


FIG. 4. **Negative mass effect on polariton dynamics.** **a**, Schematic of the creation of polaritons in real space (red) by a tight pump laser (green). The polaritons move away from the pump spot with a certain group velocity  $\mathbf{v}_g$  (red arrows). A real space filter (dashed box) is used to isolate the detection area in real space before Fourier-transforming to measure the momentum space distribution. **b-d**, Experimental results for different configurations. The upper panel shows the position of the filter with respect to the pump spot (arrows represent the average  $\mathbf{v}_g$  along the  $x$ -direction inside the detection window), the middle panel shows the angle-resolved spectra along  $k_x$ , and the bottom panel shows the momentum distribution of the (black) lower and the (red) upper branch. The fitted upper and lower polariton branches extracted from Fig. 3b are shown on top of the dispersion measurements for guidance.

with the extracted peak energies of the lower and upper exciton-polariton branches. The observed PL intensities are dictated by the photonic Hopfield coefficients and thermalisation of polaritons [34]. Hence, the PL of the upper branch, which is highly photonic at positive  $\Delta_0$ , strongly dominates the emission of the structure and decreases at larger energies due to thermalisation. To highlight the emission of the lower polariton branch, we scaled the maximum value of the PL spectrum to unity at each value of  $k$  below the cut-off energy  $E \approx 2.028$  eV. As seen in Fig. 3b, the lower branch energy decreases towards  $E_x$  at large momenta, demonstrating the level attraction shown in Fig. 2a. The complex-valued dispersion branches are extracted by fitting the spectrum at each value of  $k$  using a two-peak Voigt function, with the peak energy and linewidth corresponding to the real and imaginary parts of the complex eigenvalues of the system Hamiltonian, respectively. The peak positions can be well fitted using the model Eq. 1 with  $\Delta \approx 55$  meV,  $\gamma_x \approx 39$  meV,  $\gamma_c \approx 1.1$  meV, and the coupling constants  $V \approx 7.7$  meV and  $g \approx 31$  meV.

With  $2V > |\delta| \approx 7$  meV, the sample operates in the strong coupling regime and thus hosts exciton polaritons. However, due to the suppressed exciton oscillator strength in our sample [22] the coupling strength  $V$  is much smaller than  $g$ . Therefore, the level attraction at larger  $\Delta$  dominates, endowing a negative mass  $m_1$  to the lower polaritons with momenta larger than  $k \approx \pm 2 \mu\text{m}^{-1}$  (see Fig. 3c).

The dissipative coupling causing the observed effects

can arise from the coupling of both excitons and photons to the same decay channel [21], or to a third dissipative mode [35]. For TMDCs, such as  $\text{WS}_2$ , this coupling likely arises from the strong exciton-phonon coupling [24, 25, 36] as shown by our microscopic theory (see Supplementary Information). This is also supported by recent experimental work demonstrating the significant role of phonons in exciton-photon interaction [26]. Dissipative coupling can also arise via coupling to a ‘hidden’ photon mode [35], but this mode with opposite polarisation is not present in our planar DBR-based microcavities. We note that similarly to cavity magnonics and optomechanics, dissipative coupling might be ubiquitous in exciton-photon systems and hence, the anomalous dispersion observed here could also be observed in other materials, e.g. perovskites [16, 37] and organic semiconductors [38].

Finally, we show that the anomalous dispersion has a dramatic effect on the dynamics of the lower polaritons. In contrast to positive mass particles, such as the upper polaritons, negative-mass particles move in the opposite direction to their momentum  $\hbar\mathbf{k}$ , i.e. their group velocity is opposite to their momentum, as given by the relation  $m_1\mathbf{v}_g = \hbar\mathbf{k}$ . To demonstrate this behaviour in the experiment, we excite the sample with a tightly focused off-resonant laser spot, which results in a spatially localised distribution of polaritons with a wide range of momenta, as shown by the distributions in Fig. 3b. Polaritons will then move away from the excitation spot in the direction determined by their group velocity  $\mathbf{v}_g$



(see Fig. 4a). Hence, polaritons displaced to the positive (negative)  $x$  direction with respect to the spot must have an average velocity towards the same direction [39]. We then measure the momentum distribution of the polaritons displaced from the laser spot by Fourier transforming only a small region in real space (see Fig. 4b-d) using a spatial filter (see Methods).

Polaritons directly at the excitation spot, measured with a filter centered on the spot (see top of Fig. 4c), feature a symmetric momentum distribution for both upper and lower branches, as shown by the momentum-resolved PL spectrum (middle panel) in Fig. 4c. This is clearly seen in the lower panel, where we directly plot the momentum distribution of the two branches by separating the spectrum at  $\sim 2.02$  eV. The PL spectrum shows a dramatic change in the distribution for particles displaced to the right of the spot, as shown in Fig. 4b. The upper polariton emission is skewed to the right, i.e., the average momentum has the same direction as its group velocity, but remarkably, the lower polariton emission is skewed to the left, i.e., its average momentum is opposite to the particle displacement or the group velocity. The additional peak to the left of the upper polariton distribution likely arises from the tail of the lower polariton distribution, which has a much larger linewidth. This opposite behaviour of momentum and group velocity of the lower polaritons is consistently observed to the left of the laser spot, as demonstrated by Fig. 4d, where the particles displaced to the left, or with leftward group velocity, have the opposite, rightward average momentum. In all configurations, the upper polariton branch with the positive mass behaves as expected, i.e. the group velocity and momentum are parallel. Therefore, we have confirmed the negative-mass dynamics of the polaritons using a mixture of particles with distinct signs of effective masses  $m_1$ .

In summary, we have observed dissipative coupling of excitons and photons in a monolayer TMDC (WS<sub>2</sub>) embedded in a planar microcavity at room temperature. This coupling drastically modifies the dispersion of the coupled exciton-photon system, leading to an anomalous (inverted) dispersion for the lower polariton branch. The anomalous dispersion arises when the dissipative coupling between excitons and cavity photons overcomes their coherent coupling, which leads to a negative-mass regime in a large range of momenta at a positive exciton-photon detuning. We have demonstrated the negative-mass effect on the dynamics of polaritons, resulting in the opposing directions of group velocity and momentum.

Our work extends the arsenal of dispersion engineering tools for hybrid light-matter particles beyond the application of periodic fields and spin-orbit coupling [2, 4] by adding the possibility of novel, non-Hermitian dispersion engineering. Here, we only showed the dynamics induced by negative  $m_1$ . However, the anomalous dispersion can be further employed to demonstrate nontrivial

wavepacket dynamics [32] and negative-mass hydrodynamics [4] due to both negative  $m_1$  and  $m_2$ . For example, the negative-mass polaritons are expected to accelerate in the direction opposite to an applied force. It would be interesting to study bosonic condensation of polaritons in the anomalous dispersion regime, where the energy minimum around  $k = 0$  (see Fig. 2c) is not the global one. The inverted dispersion can also eliminate instabilities of exciton-polariton condensates [5], which can, for example, enable studies of the Kardar-Parisi-Zhang phase in quantum systems without the complexities of an underlying lattice structure [40].

**Methods:** The DBRs are grown by plasma-enhanced chemical vapour deposition (PECVD) and consist of (bottom) 17.5 and (top) 15.5 alternating quarter-wave stack of SiO<sub>x</sub> and SiN<sub>x</sub>, as schematically shown in Fig. 3a. Further, the first half of the SiO<sub>2</sub> cavity spacer is deposited via RF-sputtering and finished with atomic layer deposition (ALD). The monolayer is then mechanically transferred at 120°C on top of the oxygen-plasma treated DBR substrate to increase the bonding between the monolayer and the substrate. To protect the monolayer against further material deposition, a 70 nm thick layer of poly-methyl-methacrylate (PMMA) is spin-coated on top of the structure. Before depositing the top DBR via PECVD to complete the structure, the cavity thickness and hence, the cavity mode, is fine-tuned with an intermediate PECVD grown SiO<sub>x</sub> layer. The two DBRs enable a Q-factor of above 10<sup>3</sup> (see Supplementary Information). More details about the fabrication process are reported in Ref. [22].

The microcavity is excited with a frequency doubled Nd:YAG laser source at  $\lambda = 532$  nm ( $E \approx 2.33$  eV), which is tightly focused onto the sample surface with a infinity corrected Mitutoyo NIR objective (NA=0.65). The PL is collected with an in-house built optical microscope, which allows for spatial filtering with a square edge-filter prior to momentum-resolved imaging. The momentum-resolved PL-spectra are recorded with an Andor Shamrock 500i spectrograph equipped with an Andor iXon 888 EMCCD camera.

---

\* [matthias.wurdack@anu.edu.au](mailto:matthias.wurdack@anu.edu.au)

† [elena.ostrovskaya@anu.edu.au](mailto:elena.ostrovskaya@anu.edu.au)

‡ [eliezer.estrecho@anu.edu.au](mailto:eliezer.estrecho@anu.edu.au)

- [1] Tsakmakidis, K. L., Hess, O., Boyd, R. W. & Zhang, X. Ultraslow waves on the nanoscale, *Science* **358**, 6361 (2017).
- [2] W. Kuehn, Gaal, P., Reimann, K., Woerner, M., Elsaesser, T. & Hey, R. Coherent Ballistic Motion of Electrons in a Periodic Potential, *Phys. Rev. Lett.* **104**, 146602 (2010).
- [3] Tucker, M.A.H. & Wyatt, A.F.G. Direct evidence for R<sup>-</sup>

- rotons having antiparallel momentum and velocity, *Science* **283**, 1150 (1999).
- [4] Kamehchi, M.A., Hossain, Kh., Mossman, M.E., Zhang, Y., Busch, Th., Forbes, McNeil Forbes, M. & Engels, P., Negative-mass hydrodynamics in a spin-orbit-coupled Bose-Einstein condensate, *Phys. Rev. Lett.* **118**, 155301 (2017).
  - [5] Baboux, F., De Bernardis, D., Goblot, V., Gladilin, V. N., Gomez, C., Galopin, E., Le Gratiet, L., Lemaître, A., Sagnes, I., Carusotto, I., Wouters, M., Amo, A. & Bloch, J. Unstable and stable regimes of polariton condensation. *Optica*, **5**, 1163-1170 (2018).
  - [6] Kavokin, A. V., Baumberg, J. J., Malpuech, G. & Laussy, F. P. *Microcavities* (Oxford Univ. Press, Oxford, 2017).
  - [7] Wang, Q. H., Kalantar-Zadeh, K., Kis, A., Coleman, J. N. & Strano, M. S. Electronics and optoelectronics of two-dimensional transition metal dichalcogenides. *Nat. Nanotech.* **7**, 699-712 (2012).
  - [8] El-Ganainy, R., Khajavikhan, M., Christodoulides, D. N. & Özdemir, Ş. K. The dawn of non-Hermitian optics. *Comm. Phys.* **2**, 37 (2019).
  - [9] Miri, M.-A. & Alù, A. Exceptional points in optics and photonics. *Science* **363**, eaar7709 (2019).
  - [10] Özdemir, Ş. K., Rotter, S., Nori, F. & Yang, L. Parity-time symmetry and exceptional points in photonics. *Nat. Mater.* **18**, 783 (2019).
  - [11] Gao, T., Estrecho, E., Bliokh, K.Y., Liew, T.C.H., Fraser, M.D., Brodbeck, S., Kamp, M., Schneider, C., Höfling, S., Yamamoto, Y., Nori, F., Kivshar, Y.S., Truscott, A., Dall, R. & Ostrovskaya, E.A. Observation of non-Hermitian degeneracies in a chaotic exciton-polariton billiard. *Nature* **526**, 554 (2015).
  - [12] Gao, T., Li, G., Estrecho, E., Liew, T. C. H., Comber-Todd, D., Nalitov, A., Steger, M., West, K., Pfeiffer, L., Snoke, D., Kavokin, A. V., Truscott, A. G. & Ostrovskaya, E. A. Chiral modes at exceptional points in exciton-polariton quantum fluids, *Phys. Rev. Lett.* **120**, 065301 (2018).
  - [13] Li, Y., Ma, X., Hatzopoulos, Z., Savvidis, P., Schumacher, S. & Gao, T. Switching off microcavity polariton condensate near the exceptional point, arXiv:2101.09478 (2021).
  - [14] Pickup, L., Sigurdsson, H., Ruostekoski, J. & Lagoudakis, P. G. Synthetic band-structure engineering in polariton crystals with non-Hermitian topological phases. *Nat Commun.* **11**, 4431 (2020).
  - [15] Pernet, N., P. St-Jean, P., Solnyshkov, D. D., Malpuech, G., Carlon Zambon, N., Real, B., Jamadi, O., Lemaître, A., Morassi, M., Le Gratiet, L., Baptiste, T., Harouri, Sagnes, I., Amo, A., Ravets, S & Bloch, J. Topological gap solitons in a 1D non-Hermitian lattice, arXiv:2101.01038 (2021).
  - [16] Su, R., Estrecho, E., Bieganska, D., Huang, Y., Wurdack, M., Pieczarka, M., Truscott, A. G., Liew, T.C.H., Ostrovskaya, E. A. & Xiong, Q. Direct Measurement of a Non-Hermitian Topological Invariant in a Hybrid Light-Matter System, *Science Advances* **7**, 45 (2021).
  - [17] Liao, Q., Leblanc, Ch., Ren, J., Li, F., Li, Y., Solnyshkov, D., Malpuech, G., Yao, J. & Fu, H. Experimental measurement of the divergent quantum metric of an exceptional point, *Phys. Rev. Lett.* **127**, 107402 (2021).
  - [18] Elste, F., Girvin, S. M., & Clerk, A. A. Quantum Noise Interference and Backaction Cooling in Cavity Nanomechanics. *Phys. Rev. Lett.* **102**, 207209 (2009).
  - [19] Okołowicz, J., Płoszajczak, M., and Rotter, I., Dynamics of quantum systems embedded in a continuum, *Physics Reports* **374**, 271 (2003).
  - [20] Harder, M., Yang, Y., Yao, B. M., Yu, C. H., Rao, J. W., Gui, Y. S., Stamps, R. L., & Hu, C.-M. Level Attraction Due to Dissipative Magnon-Photon Coupling. *Phys. Rev. Lett.* **121**, 137203 (2018).
  - [21] Persson, E., Rotter, I., Stöckmann, H.-J., & Barth, M. Observation of Resonance Trapping in an Open Microwave Cavity. *Phys. Rev. Lett.* **85**, 2478 (2000).
  - [22] Yun, T., Estrecho, E., Truscott, A. G., Ostrovskaya, E. A. & Wurdack, M. Fabrication of high-quality PMMA/SiO<sub>x</sub> spaced planar microcavities for strong coupling of light with monolayer WS<sub>2</sub> excitons. arXiv:2204.01181 (2022)
  - [23] Selig, M., Berghäuser, G., Raja, A., Nagler, P., Schüller, C., Heinz, T. F., Korn, T., Chernikov, A., Malic, E. & Knorr, A. Excitonic linewidth and coherence lifetime in monolayer transition metal dichalcogenides. *Nat. Commun.* **7**, 13279 (2016).
  - [24] Moody, G., Dass, C. K., Hao, K., Chen, C.-H., Li, L.-J., Singh, A., Tran, K., Clark, G., Xu, X., Berghäuser, G., Malic, E., Knorr, A., and Li, X., Intrinsic homogeneous linewidth and broadening mechanisms of excitons in monolayer transition metal dichalcogenides, *Nat. Commun.* **6**, 8315 (2015).
  - [25] Li, D., Trovatiello, C., Dal Conte, S., Nuß, M., Soavi, G., Wang, G., Ferrari, A. C., Cerullo, G., and Brixner, T., Exciton-phonon coupling strength in single-layer MoSe<sub>2</sub> at room temperature, *Nat. Commun.* **12**, 954 (2021).
  - [26] Li, D., Shan, H., Rupprecht, C., Knopf, H., Watanabe, K., Taniguchi, T., Qin, Y., Tongay, S., Nuss, M., Schröder, S., Eilenberger, Fl., Höfling, S., Schneider C., and Brixner, T., Hybridized Exciton-Photon-Phonon States in a Transition Metal Dichalcogenide, *Phys. Rev. Lett.* **128**, 087401 (2022).
  - [27] I. L. Aleiner, I. L., Altshuler, B. L. & Rubo Y. G., Radiative coupling and weak lasing of exciton-polariton condensates. *Phys. Rev. B* **85**, 121301(R) (2012).
  - [28] Kyriienko, O., Liew, T. C. H., and Shelykh, I. A., Optomechanics with Cavity Polaritons: Dissipative Coupling and Unconventional Bistability, *Phys. Rev. Lett.* **112**, 076402 (2014).
  - [29] Weisbuch, C., Nishioka, M., Ishikawa, A. & Arakawa, Y. Observation of the coupled exciton-photon mode splitting in a semiconductor quantum microcavity, *Phys. Rev. Lett.* **69**, 3314-3317 (1992).
  - [30] Deng, H., Haug, H. & Yamamoto, Y. Exciton-polariton Bose-Einstein condensation, *Rev. Mod. Phys.* **82**, 1489-1537 (2010).
  - [31] Liu, X., Galfsky, T., Sun, Z., Xia, F., Lin, E., Lee, Y.-H., Kena-Cohen, S. & Menon, V. M. Strong light-matter coupling in two-dimensional atomic crystals. *Nat. Photon.* **9**, 30-34 (2015).
  - [32] Colas, D., Laussy, F. P. & Davis, M. J. Negative-mass effects in spin-orbit coupled Bose-Einstein condensates, *Phys. Rev. Lett.* **121**, 055302 (2018).
  - [33] Dhara, S., Chakraborty, C., Goodfellow, K., Qiu, L., O'Loughlin, T. A., Wicks, G. W., Bhattacharjee, S. & Vamivakas, A. N. Anomalous dispersion of microcavity trion-polaritons. *Nat. Phys.* **14**, 130-133 (2018).
  - [34] Lundt, N., Klemmt, S., Cherotchenko, E., Betzold, S., Iff, O., Nalitov, A. V., Klaas, M., Dietrich, C. P., Kavokin,

- A. V., Höfling, S. & Schneider, C. Room-temperature Tamm-plasmon exciton-polaritons with a WSe<sub>2</sub> monolayer. *Nat. Commun.* **7**, 13328 (2016).
- [35] Yu, W., Wang, J., Yuan, H. Y., & Xiao, J. Prediction of Attractive Level Crossing via a Dissipative Mode. *Phys. Rev. Lett.* **123**, 227201 (2019).
- [36] Christiansen, D., Selig, M., Berghäuser, G., Schmidt, R., Niehues, I., Schneider, R., Arora, A., Michaelis de Vasconcellos, S., Bratschitsch, R., Malic, E. and Knorr, A., Phonon Sidebands in Monolayer Transition Metal Dichalcogenides, *Phys. Rev. Lett.* **119**, 187402 (2017).
- [37] Su, R., Ghosh, S., Wang, J., Liu, S., Diederichs, C., Liew, T. C. H. & Xiong, Q. Observation of exciton polariton condensation in a perovskite lattice at room temperature. *Nat. Phys.* **16**, 301-306 (2020).
- [38] Plumhof, J. D., Stöferle, T., Mai, L., Scherf, U. & Mahrt, R. F. Room-temperature Bose-Einstein condensation of cavity exciton-polaritons in a polymer. *Nat. Mater.* **13**, 247-252 (2014).
- [39] Wurdack, M. Estrecho, E., Todd, S., Yun, T., Pieczarka, M., Earl, S. K., Davis, J. A., Schneider, C., Truscott, A. G., and Ostrovskaya, E. A., Motional narrowing, ballistic transport, and trapping of room-temperature exciton polaritons in an atomically-thin semiconductor. *Nat. Commun.* **12**, 5366 (2021).
- [40] Fontaine, Q., Squizzato, D., Baboux, F., Amelio, I., Lemaître, A., Morassi, M., Sagnes, I., Gratiet L.L., Harouri, A., Wouters, M., Carusotto, I., Amo, A., Richard, M., Minguzzi, A., Canet, L., Ravets, S., and Bloch, J., Observation of KPZ universal scaling in a one-dimensional polariton condensate, *arXiv* 2112.09550 (2021).

# Negative-mass exciton polaritons induced by dissipative light-matter coupling in an atomically thin semiconductor

## Supplementary Information

M. Wurdack,<sup>1,\*</sup> T. Yun,<sup>1,2</sup> M. Katzer,<sup>3</sup> A. G. Truscott,<sup>4</sup> A. Knorr,<sup>3</sup> M. Selig,<sup>3</sup> E. A. Ostrovskaya,<sup>1,†</sup> and E. Estrecho<sup>1,‡</sup>

<sup>1</sup>ARC Centre of Excellence in Future Low-Energy Electronics Technologies and Nonlinear Physics Centre, Research School of Physics, The Australian National University, Canberra, ACT 2601, Australia

<sup>2</sup>Department of Materials Science and Engineering, Monash University, Clayton, Victoria, 3800, Australia

<sup>3</sup>Nichtlineare Optik und Quantenelektronik, Institut für Theoretische Physik, Technische Universität Berlin, 10623 Berlin, Germany

<sup>4</sup>Laser Physics Centre, Research School of Physics, The Australian National University, Canberra, ACT 2601, Australia

### S1: MICROSCOPICAL CALCULATIONS OF THE POLARITON DISPERSION

In order to self-consistently compute both the polariton dispersion and dephasing, we consider a microscopic Hamiltonian, containing excitons (X), phonons (b), as well as resonator- (C) and reservoir photons (D), including their individual coupling

$$H = H_0 + H_{X-Phon} + H_{X-Phot} + H_{Phot-Phot}, \quad (1)$$

Here, the free contributions of the different species read  $H_0 = \sum_{\mathbf{Q}_{\parallel},\sigma} E_{\mathbf{Q}_{\parallel}}^X X_{\mathbf{Q}_{\parallel}}^{\dagger\sigma} X_{\mathbf{Q}_{\parallel}}^{\sigma} + \sum_{\mathbf{K}_{\parallel},\alpha} \hbar\omega_{\mathbf{K}_{\parallel}}^{\alpha} b_{\mathbf{K}_{\parallel}}^{\dagger\alpha} b_{\mathbf{K}_{\parallel}}^{\alpha} + \sum_{\mathbf{Q}_{\parallel},\sigma} E_{\mathbf{Q}_{\parallel}}^C C_{\mathbf{Q}_{\parallel}}^{\dagger\sigma} C_{\mathbf{Q}_{\parallel}}^{\sigma} + \sum_{\mathbf{Q},\tau} E_{\mathbf{Q}}^D D_{\mathbf{Q}}^{\dagger\tau} D_{\mathbf{Q}}^{\tau}$ , where the first term accounts for the dispersion of excitons  $E_{\mathbf{Q}_{\parallel}}^X = E_0^X + \frac{\hbar^2 \mathbf{Q}_{\parallel}^2}{2M}$  with the spectral energy  $E_0^X$ , the mass  $M$  [1] of the exciton and the two dimensional center of mass momentum  $\mathbf{Q}_{\parallel}$ .  $X_{\mathbf{Q}_{\parallel}}^{(\dagger)\sigma}$  denote exciton annihilation (creation) operators with the valley  $\sigma = K, K' = +, -$ , which we assume to commute as bosons in the zero density limit. The second term of  $H_0$  denotes the phonon dispersion  $\hbar\omega_{\mathbf{K}_{\parallel}}^{\alpha}$  obtained from DFT calculations [2, 3]. Furthermore  $b_{\mathbf{K}_{\parallel}}^{(\dagger)\alpha}$  denote phonon annihilation (creation) operators. The third term accounts for the dispersion of the photons in the cavity  $E_{\mathbf{Q}_{\parallel}}^C = \sqrt{(E_0^C)^2 + \frac{\hbar^2 c^2 \mathbf{Q}_{\parallel}^2}{(n^C)^2}}$ , with the confinement energy  $E_0^C = \frac{\hbar c}{2n^C d^C}$  adjusted to the experiment (see section S5), the speed of light  $c$ , the cavity refractive index  $n^C$  and the cavity length  $d^C$ . Photon annihilation (creation) operators in the cavity are denoted by  $C_{\mathbf{Q}_{\parallel}}^{(\dagger)\sigma}$  with the photon polarization  $\sigma = \sigma_+, \sigma_- = +, -$ . The last term describes the dispersion of the free photons outside of the cavity  $E_{\mathbf{Q}}^D = \frac{\hbar c |\mathbf{Q}|}{n^D}$ .

The exciton-phonon interaction Hamiltonian is given as  $H_{X-Phon} = \sum_{\mathbf{Q}_{\parallel}, \mathbf{K}_{\parallel}, \alpha, \sigma} g_{\mathbf{K}_{\parallel}}^{\alpha} X_{\mathbf{Q}_{\parallel}+\mathbf{K}_{\parallel}}^{\dagger\sigma} X_{\mathbf{Q}_{\parallel}}^{\sigma} (b_{\mathbf{K}_{\parallel}}^{\alpha} + b_{-\mathbf{K}_{\parallel}}^{\dagger\alpha})$  with the exciton-phonon matrix element  $g_{\mathbf{K}_{\parallel}}^{\alpha}$  [2-4]. The exciton-photon coupling Hamiltonian in rotating wave approximation with the excitonic dipole moment  $\mathbf{d}$  [5, 6] is given as  $H_{X-Phot} = \sum_{\mathbf{Q}_{\parallel},\sigma} V_{\mathbf{Q}_{\parallel}} (X_{-\mathbf{Q}_{\parallel}}^{\dagger\sigma} C_{-\mathbf{Q}_{\parallel}}^{\sigma} + X_{\mathbf{Q}_{\parallel}}^{\sigma} C_{\mathbf{Q}_{\parallel}}^{\dagger\sigma})$ .

The appearing exciton-photon matrix element reads

$V_{\mathbf{Q}_{\parallel}} = \sqrt{\frac{E_{\mathbf{Q}_{\parallel}}^L}{\epsilon_0 I^{\frac{1}{2}}}} \sin(\frac{\pi z}{d}) \mathbf{e}^{\sigma} \cdot \mathbf{d}$  (the appearing  $\delta_{\mathbf{Q}_{\parallel}, \mathbf{Q}_{\parallel}}$  was already accounted for). In order to describe the out-coupling of cavity photons to the vacuum, we write the phenomenological tunneling Hamiltonian  $H_{Phot-Phot} = \sum_{\mathbf{Q}\sigma\tau} T_{\mathbf{Q}}^{\sigma\tau} (C_{\mathbf{Q}_{\parallel}}^{\sigma} D_{\mathbf{Q}}^{\dagger\tau} + C_{-\mathbf{Q}_{\parallel}}^{\dagger\sigma} D_{-\mathbf{Q}}^{\tau})$ . The Heisenberg equation of motion formalism allows to find a closed set of linear equations, namely the equations of motion (EOM) for the coherent exciton amplitude  $\langle X_{\mathbf{Q}_{\parallel}}^{\sigma} \rangle$ , the coherent cavity photon amplitude  $\langle C_{\mathbf{Q}_{\parallel}}^{\sigma} \rangle$  and the coherent amplitude of the free photons outside the cavity  $\langle D_{\mathbf{Q}}^{\tau} \rangle$ . To close the system, it is necessary to also compute equations of the respective phonon assisted amplitudes  $\langle X_{\mathbf{Q}_{\parallel}}^{\sigma} b_{\mathbf{K}_{\parallel}}^{(\dagger)\alpha} \rangle$ ,  $\langle C_{\mathbf{Q}_{\parallel}}^{\sigma} b_{\mathbf{K}_{\parallel}}^{(\dagger)\alpha} \rangle$  and  $\langle D_{\mathbf{Q}}^{\tau} b_{\mathbf{K}_{\parallel}}^{(\dagger)\alpha} \rangle$ . Reflecting the strong coupling between excitons and cavity photons, the whole set of EOM is diagonalised with respect to the coupling  $M_{\mathbf{Q}_{\parallel}}$ , which gives  $X_{\mathbf{Q}_{\parallel}}^{\sigma} = \alpha_{\mathbf{Q}_{\parallel}} P_{\mathbf{Q}_{\parallel}\sigma}^{-} + \beta_{\mathbf{Q}_{\parallel}} P_{\mathbf{Q}_{\parallel}\sigma}^{+}$ , and  $C_{\mathbf{Q}_{\parallel}}^{\sigma} = \alpha_{\mathbf{Q}_{\parallel}} P_{\mathbf{Q}_{\parallel}\sigma}^{+} - \beta_{\mathbf{Q}_{\parallel}} P_{\mathbf{Q}_{\parallel}\sigma}^{-}$ , with the coherent amplitudes of the (upper and lower) polariton branches  $P_{\mathbf{Q}_{\parallel}\sigma}^{\pm}$  and the complex Hopfield coefficients

$$\alpha_{\mathbf{Q}_{\parallel}}, \beta_{\mathbf{Q}_{\parallel}} = \frac{1}{\sqrt{2}} \sqrt{1 \pm \frac{\tilde{\Delta}_{\mathbf{Q}_{\parallel}}}{\sqrt{\tilde{\Delta}_{\mathbf{Q}_{\parallel}}^2 + 4\tilde{V}_{\mathbf{Q}_{\parallel}}^2}}}, \text{ with the energy}$$

detuning  $\tilde{\Delta}_{\mathbf{Q}_{\parallel}} = E_{\mathbf{Q}_{\parallel}}^C - E_{\mathbf{Q}_{\parallel}}^X - i(\gamma_{\mathbf{Q}_{\parallel}}^C - \gamma_{\mathbf{Q}_{\parallel}}^X)$  and the complex coupling between excitons and cavity photons  $\tilde{V}_{\mathbf{Q}_{\parallel}} = V_{\mathbf{Q}_{\parallel}} + ig_{\mathbf{Q}_{\parallel}}$ . Note that both  $\tilde{\Delta}_{\mathbf{Q}_{\parallel}}$  and  $\tilde{V}_{\mathbf{Q}_{\parallel}}$  are complex terms, with the real parts stemming directly from the Hamiltonians for dispersion and exciton-photon interaction, respectively. The imaginary parts are however to be found as the solution vector  $(\gamma_{\mathbf{Q}_{\parallel}}^X, \gamma_{\mathbf{Q}_{\parallel}}^C, g_{\mathbf{Q}_{\parallel}})$  of the self consistent EOM, as will be shown in the following. After diagonalisation, the EOM of the phonon assisted quantities can be solved subsequently in a Born-Markov approach, (for  $\langle X_{\mathbf{Q}_{\parallel}}^{\sigma} b_{\mathbf{K}_{\parallel}}^{(\dagger)\alpha} \rangle$  even a second diagonalisation is necessary). Eventually, we



end up with

$$\begin{aligned} & \left( i\hbar\partial_t - E_{\mathbf{Q}_{\parallel}}^+ + i\alpha_{\mathbf{Q}_{\parallel}}^2 \Gamma_{\mathbf{Q}_{\parallel}}^{Pt+} + i\beta_{\mathbf{Q}_{\parallel}}^2 \Gamma_{\mathbf{Q}_{\parallel}}^{Pn+} \right) \langle P_{\mathbf{Q}_{\parallel}\sigma}^+ \rangle \\ & - i\alpha_{\mathbf{Q}_{\parallel}} \beta_{\mathbf{Q}_{\parallel}} (\Gamma_{\mathbf{Q}_{\parallel}}^{Pt-} - \Gamma_{\mathbf{Q}_{\parallel}}^{Pn-}) \langle P_{\mathbf{Q}_{\parallel}\sigma}^- \rangle = \beta_{\mathbf{Q}_{\parallel}} \Omega_{\mathbf{Q}_{\parallel}}^{\sigma} \quad (2) \end{aligned}$$

$$\begin{aligned} & \left( i\hbar\partial_t - E_{\mathbf{Q}_{\parallel}}^- + i\beta_{\mathbf{Q}_{\parallel}}^2 \Gamma_{\mathbf{Q}_{\parallel}}^{Pt-} + i\alpha_{\mathbf{Q}_{\parallel}}^2 \Gamma_{\mathbf{Q}_{\parallel}}^{Pn-} \right) \langle P_{\mathbf{Q}_{\parallel}\sigma}^- \rangle \\ & - i\alpha_{\mathbf{Q}_{\parallel}} \beta_{\mathbf{Q}_{\parallel}} (\Gamma_{\mathbf{Q}_{\parallel}}^{Pt+} - \Gamma_{\mathbf{Q}_{\parallel}}^{Pn+}) \langle P_{\mathbf{Q}_{\parallel}\sigma}^+ \rangle = \alpha_{\mathbf{Q}_{\parallel}} \Omega_{\mathbf{Q}_{\parallel}}^{\sigma}. \quad (3) \end{aligned}$$

Where  $\Omega_{\mathbf{Q}_{\parallel}}^{\sigma}$  accounts for the external driving, and the microscopically derived dephasing due to the photonic reservoir outside the cavity reads  $\Gamma_{\mathbf{Q}_{\parallel}}^{Pt\pm} = \pi \sum_{Q_z, \tau\sigma} (T_{\mathbf{Q}_{\parallel}}^{\sigma\tau})^2 \delta(E_{\mathbf{Q}_{\parallel}}^D - E_{\mathbf{Q}_{\parallel}}^{\pm})$  and the derived dephasing due to the phonons in the

TMDC can be written as  $\Gamma_{\mathbf{Q}_{\parallel}}^{Pn\pm} = \pi \sum_{\mathbf{K}_{\parallel}, \alpha} |g_{|\mathbf{K}_{\parallel} - \mathbf{Q}_{\parallel}|}^{\alpha}|^2 \left( \bar{\alpha}_{\mathbf{K}_{\parallel}}^2 (1 + n_{|\mathbf{K}_{\parallel} - \mathbf{Q}_{\parallel}|}^{\alpha}) \delta(\mathcal{E}_{\mathbf{K}_{\parallel}}^L - E_{\mathbf{Q}_{\parallel}}^{\pm} + \hbar\omega_{|\mathbf{K}_{\parallel} - \mathbf{Q}_{\parallel}|}^{\alpha}) \right. \\ + \bar{\alpha}_{\mathbf{K}_{\parallel}}^2 n_{|\mathbf{K}_{\parallel} - \mathbf{Q}_{\parallel}|}^{\alpha} \delta(\mathcal{E}_{\mathbf{K}_{\parallel}}^L - E_{\mathbf{Q}_{\parallel}}^{\pm} - \hbar\omega_{|\mathbf{K}_{\parallel} - \mathbf{Q}_{\parallel}|}^{\alpha}) \\ + \bar{\beta}_{\mathbf{K}_{\parallel}}^2 (1 + n_{|\mathbf{K}_{\parallel} - \mathbf{Q}_{\parallel}|}^{\alpha}) \delta(\mathcal{E}_{\mathbf{K}_{\parallel}}^U - E_{\mathbf{Q}_{\parallel}}^{\pm} + \hbar\omega_{|\mathbf{K}_{\parallel} - \mathbf{Q}_{\parallel}|}^{\alpha}) \\ \left. + \bar{\beta}_{\mathbf{K}_{\parallel}}^2 n_{|\mathbf{K}_{\parallel} - \mathbf{Q}_{\parallel}|}^{\alpha} \delta(\mathcal{E}_{\mathbf{K}_{\parallel}}^U - E_{\mathbf{Q}_{\parallel}}^{\pm} - \hbar\omega_{|\mathbf{K}_{\parallel} - \mathbf{Q}_{\parallel}|}^{\alpha}) \right),$  with the

phonon occupation  $n_{\mathbf{Q}_{\parallel}}^{\alpha} = \langle b_{\mathbf{Q}_{\parallel}}^{\dagger\alpha} b_{\mathbf{Q}_{\parallel}}^{\alpha} \rangle$  computed from a Bose-Einstein statistics for the lattice temperature. We stress that for both the photonic and the phononic dispersion channels, the Fermi-rules in the delta functions secure that all scattering events obey energy conservation with respect to the self-consistently computed exciton-polariton dispersion  $E_{\mathbf{Q}_{\parallel}}^{\pm} = \frac{E_{\mathbf{Q}_{\parallel}}^X + E_{\mathbf{Q}_{\parallel}}^C}{2} \pm \Re \left( \sqrt{\frac{\tilde{\Delta}_{\mathbf{Q}_{\parallel}}^2}{4} + \tilde{V}_{\mathbf{Q}_{\parallel}}^2} \right)$ . (The imaginary counterpart of this dispersion gives the respective dephasing in the diagonalised basis,  $\gamma_{\mathbf{Q}_{\parallel}}^{\pm} = \frac{\gamma_{\mathbf{Q}_{\parallel}}^X + \gamma_{\mathbf{Q}_{\parallel}}^C}{2} \mp \Im \left( \sqrt{\frac{\tilde{\Delta}_{\mathbf{Q}_{\parallel}}^2}{4} + \tilde{V}_{\mathbf{Q}_{\parallel}}^2} \right)$ ).

Eq. (2,3) can be mapped on a phenomenological model, where  $\langle P_{\mathbf{Q}_{\parallel}\sigma}^+ \rangle$  and  $\langle P_{\mathbf{Q}_{\parallel}\sigma}^- \rangle$  must be decoupled after diagonalisation, which gives in total four equations for the computation of the dephasing

$$\gamma_{\mathbf{Q}_{\parallel}}^+ = \alpha_{\mathbf{Q}_{\parallel}}^2 \Gamma_{\mathbf{Q}_{\parallel}}^{Pt+} + \beta_{\mathbf{Q}_{\parallel}}^2 \Gamma_{\mathbf{Q}_{\parallel}}^{Pn+} \quad (4)$$

$$\gamma_{\mathbf{Q}_{\parallel}}^- = \beta_{\mathbf{Q}_{\parallel}}^2 \Gamma_{\mathbf{Q}_{\parallel}}^{Pt-} + \alpha_{\mathbf{Q}_{\parallel}}^2 \Gamma_{\mathbf{Q}_{\parallel}}^{Pn-} \quad (5)$$

$$0 = \alpha_{\mathbf{Q}_{\parallel}} \beta_{\mathbf{Q}_{\parallel}} (\Gamma_{\mathbf{Q}_{\parallel}}^{Pt-} - \Gamma_{\mathbf{Q}_{\parallel}}^{Pn-}) \quad (6)$$

$$0 = \alpha_{\mathbf{Q}_{\parallel}} \beta_{\mathbf{Q}_{\parallel}} (\Gamma_{\mathbf{Q}_{\parallel}}^{Pt+} - \Gamma_{\mathbf{Q}_{\parallel}}^{Pn+}) \quad (7)$$

This set of equations completely determines the dephasing, which means that its solution gives the dephasing also in the original basis, i.e.  $\gamma_{\mathbf{Q}_{\parallel}}^X$  as the dephasing of the excitons,  $\gamma_{\mathbf{Q}_{\parallel}}^C$  as the respective dephasing of the cavity photons, and a third dephasing  $g_{\mathbf{Q}_{\parallel}}$ , which corresponds to the imaginary part of  $\tilde{V}_{\mathbf{Q}_{\parallel}}$  and is off-diagonal in the original basis of the Hamiltonian. Those three parts of the dephasing constitute a vector of numerical solutions of Eqs. (4-7). Since  $\Gamma_{\mathbf{Q}_{\parallel}}^{Pt\pm} = \Gamma_{\mathbf{Q}_{\parallel}}^{Pn\pm}$  is unlikely, we reduce Eqs. (6,7) to the more likely scenario  $\alpha_{\mathbf{Q}_{\parallel}} \beta_{\mathbf{Q}_{\parallel}} = 0$ , which reduces the set of equations to match the

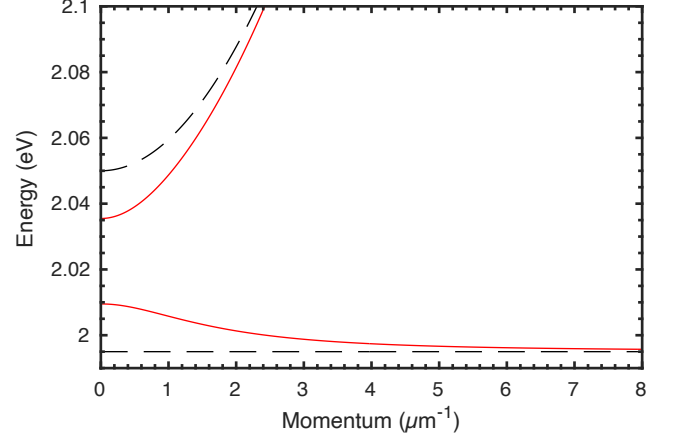


FIG. S1. Calculated dispersion of (red) the upper ( $E^+$ ) and lower ( $E^-$ ) polariton branches, and (black dashed) the dispersion of the uncoupled excitons,  $E^X$ , and of the cavity photons,  $E^C$ . The level attraction can be traced back to the off-diagonal dephasing  $g_{\mathbf{Q}_{\parallel}}$ , which is computed self consistently from the interplay of phononic dephasing in the TMDC and photonic dephasing from the cavity loss.

dimension of the solution vector  $(\gamma_{\mathbf{Q}_{\parallel}}^X, \gamma_{\mathbf{Q}_{\parallel}}^C, g_{\mathbf{Q}_{\parallel}})$ . As exciton-phonon scattering occurs at a range of momenta and energies substantially exceeding that of the light-cone and the light-matter coupling region,  $\mathbf{K}_{\parallel} \gg \mathbf{Q}_{\parallel}$ , we approximate  $\mathbf{Q}_{\parallel} \approx 0$  and  $|\mathbf{K}_{\parallel} - \mathbf{Q}_{\parallel}| \approx \mathbf{K}_{\parallel}$  [7], which significantly reduces the computational overhead. This leaves us with the solution vector  $(\gamma_0^X, \gamma_0^C, g_0)$ .

Solving this system of equations with  $V_0 = 14$  meV [8],  $E_0^C = 2.05$  eV,  $E_X = 1.995$  eV, and  $T_0 = 0.16$  eV (corresponding to a cavity linewidth of  $\Gamma_C = T_0^2/\hbar c_0 \approx 0.14$  meV), we find an off-diagonal dephasing of  $g_0 \approx 24$  meV, which exceeds its real counterpart. The computed excitonic and photonic dephasings are  $\gamma_0^X \approx 1.1$  meV and  $\gamma_0^C \approx 33$  meV. Note, that these solutions are not directly related to the measured linewidths, and the physical meaning of these parameters is subject to further studies.

Fig. S1 shows the dispersion for the numerically computed values. The level attraction between upper and lower polariton branch is clearly visible. We want to stress that only when considering both a phononic reservoir for the excitons, and a reservoir of free photons outside the cavity, it can lead to nonzero off-diagonal dephasing  $g_0$  and to the two-level attraction as experimentally observed. This justifies our phenomenological formula that accounts for dissipative coupling, which reproduces well the dispersion found with the microscopic model at large exciton-photon detuning and with substantial dissipative coupling (see Fig. S3c). However, no solutions were found with maximum two-level attraction occurring at  $k \neq 0$ , as it was observed experimentally, which motivates further studies.

## S2: ENERGY LEVEL DYNAMICS IN $\Delta$ - $V$ PARAMETER SPACE

The general behaviour of the energy eigenvalues presented in the main text is further described here. Figure S2a shows the mean-subtracted energies  $E - \langle E \rangle$  in  $\Delta$ - $V$  parameter space, highlighting the position of the non-Hermitian degeneracy, the exceptional point. Without dissipative coupling, i.e. when  $g = 0$ , the exceptional point occurs at resonance  $\Delta = 0$  with the critical coherent coupling strength  $V_c = |(\gamma_c - \gamma_x)|/2$ . The dissipative coupling term  $g$  shifts the exceptional point away from resonance towards  $\Delta = 2\sqrt{g\gamma_x}$ , while counter-intuitively reducing the critical coherent coupling strength to  $V_c = |(\gamma_c + g - \gamma_x)|/2$ . This is because  $\gamma_c$  is significantly smaller than  $\gamma_x$ , so  $g$  fills in the difference, resulting in a smaller  $V_c$ .

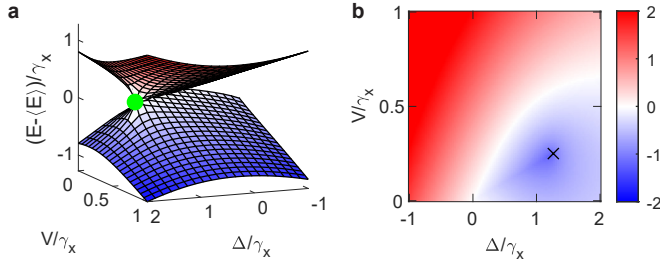


FIG. S2. **Exceptional point and energy deviation.** **a**, Mean-subtracted energy surfaces of the eigenvalue branches, and **b**, energy deviation  $\Delta_{UP}$  in the  $\Delta$ - $V$  parameter space. The exceptional point (green dot and 'x' mark) is at  $V = |(\gamma_c + g - \gamma_x)|/2$ ,  $\Delta = 2\sqrt{g\gamma_x}$ . Other parameters are:  $\gamma_c = 0.1\gamma_x$  and  $g = 0.4\gamma_x$ .

Figure S2b shows the energy deviation  $\Delta_{UP} = E_U - E_L - \Delta$  as a function of  $\Delta$  and  $V$  for  $g = 0.4\gamma_x$ . Regions in red (blue) represent level repulsion (attraction), and the white region represent the transition between them. This clearly shows that level attraction will only become apparent when  $V$  is sufficiently small. It is also important to stress that maximum level attraction (negative  $\Delta_{UP}$ ) occurs at the exceptional point, which is marked by 'x' in Fig. S2b. This is because the exceptional point (where the coupled energies cross) is shifted away from  $\Delta = 0$  (where the uncoupled energies cross), resulting in a large energy difference between the coupled and uncoupled energies.

## S3: DISPERSIONS AT ZERO AND NEGATIVE EXCITON-PHOTON DETUNINGS

Figure S3 shows supplementary exciton-photon dispersions at different detunings  $\Delta_0$  and coupling strengths  $V$  and  $g$ . The case for resonant ( $\Delta_0 = 0$ ) detuning is shown in Fig. S3a, which shows similar features as those in the main text, i.e. an inverted dispersion at finite  $k$ , when the dissipative coupling strength  $g$  is strong. The same features are exhibited by the negative detuning case in Fig. S3b, except

for the crossing in energies when  $V = 0$ , which is expected in the weak coupling regime.

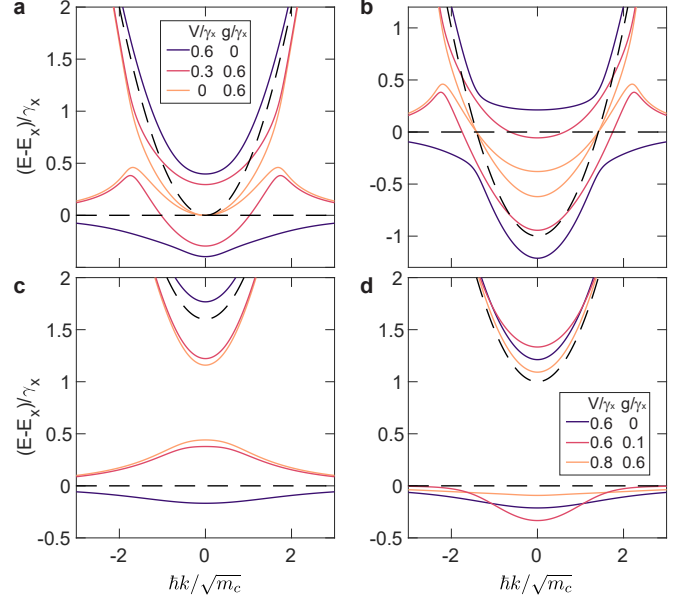


FIG. S3. **Dispersions at different exciton-photon detunings.** **a**, Zero ( $\Delta_0 = 0$ ), **b**, negative ( $\Delta_0 = -\gamma_x$ ), and **c**, highly positive ( $\Delta_0 = 2\gamma_x$ ) detunings. Dashed lines correspond to the exciton and cavity photon dispersions. The values for  $V$  and  $g$  in **b** and **c** are the same as those in **a**.

The interesting case of a very positive detuning, with  $\Delta_0 = 2\gamma_x$ , is shown in Fig. S3c, which features an inverted dispersion centred at  $k = 0$ . Here, both  $m_1$  and  $m_2$  are negative around  $k = 0$  with  $m_1$  being negative for a wide range of momenta  $\hbar k$ . Note that in the two cases with  $g = 0.6\gamma_x$ , the lower branch is blueshifted from the exciton line. The parameters here correspond to the upper region of Fig. 2f of the main text.

We also show the dispersion for the set of parameters where there is no negative  $m_1$ , as presented in Fig. S3d, corresponding to the upper and lower regions in Fig. 2d and 2e of the main text, respectively. Examples are given for the case when  $g$  is present but weak, and when  $g$  is strong but  $V$  is stronger. In both cases at positive detuning, the lower branch remains below the exciton line.

## S4: EXCEPTIONAL-POINT INDUCED ANOMALOUS DISPERSION WITHOUT DISSIPATIVE COUPLING

A similar anomalous dispersion but for exciton-photon system can also occur without dissipative coupling as demonstrated in Fig. S4a. Similar to the case presented in the main text, this can be uncovered by weakening the coherent coupling strength  $V$ , but towards the weak coupling regime, i.e.  $V < |\gamma_c - \gamma_x|/2$ . In this regime, the level repulsion has a nontrivial behaviour as a function of  $\Delta$ , as presented by the solid lines in Fig. S4b, where the level repulsion is zero at

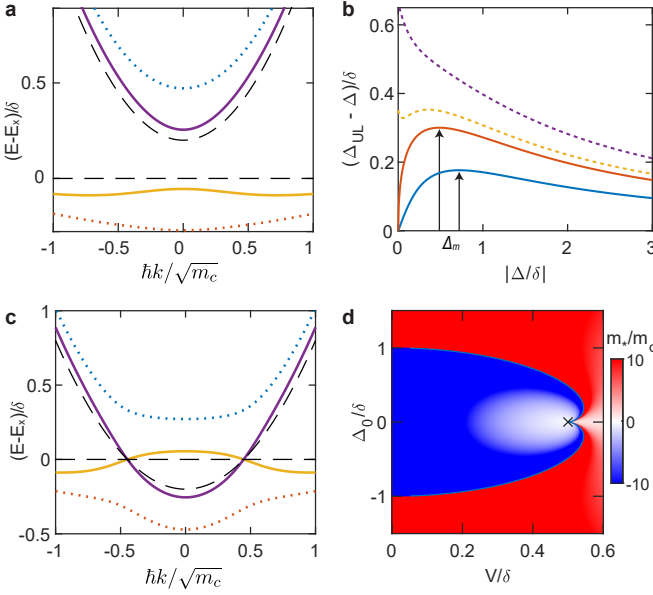


FIG. S4. **Exceptional-point induced anomalous dispersion, without dissipative coupling.** **a,c**, Exciton–photon dispersion in the weak (solid lines,  $V/|\delta| = 0.4$ ) and strong (dotted lines,  $V/|\delta| = 0.6$ ) coupling regimes. **b**, Energy deviation  $\Delta_{UP}$  in the weak (solid lines) and strong (dashed lines) coupling regimes. From bottom:  $V/|\delta| = 0.4, 0.5, 0.53, 0.6$ . **d**, Effective mass  $m^*$  at  $k = 0$  in the  $V$ - $\Delta_0$  parameter space.  $\times$  marks the exceptional point.

$\Delta = 0$  but increases to a maximum at some finite  $\Delta_m$ , then decreases again with increasing  $\Delta$ . This is in contrast to the strong coupling case (dashed lines) where the level repulsion is maximised at  $\Delta = 0$  and monotonously decrease with  $\Delta$ . With this nontrivial level dynamics, the exciton–photon dispersion will feature stronger level repulsion at finite  $k$  (around  $\Delta_m$ ) compared to those near  $k = 0$  (smaller  $\Delta$ ), resulting in a negative-mass dispersion centred at  $k = 0$ .

The effect can also persist at negative exciton–photon detuning  $\Delta_0$  but only for the exciton-like branch, as shown in Fig. S4c. The branches cross at negative  $\Delta_0$  in the weak coupling regime. The anomalous dispersion of the exciton-like branch persists for a wide range of  $\Delta_0$ , as presented by the map in Fig. S4d. Here,  $m^*$  is the effective mass at  $k = 0$ , which is the same for  $m_1$  and  $m_2$ . Interestingly, the strongest anomalous dispersion, i.e. smallest negative mass, occurs close to the exceptional point at  $V = |\gamma_c - \gamma_x|/2$  and  $\Delta = 0$ . Hence, this kind of anomalous dispersion is induced by the exceptional point, which has a square-root behaviour of energies close to it.

Note that the effect presented here cannot replicate the experimental results presented in the main text. Firstly, the inverted dispersion is always centred at  $k = 0$ , except for those cases very close to  $V = |\gamma_c - \gamma_x|/2$  at negative detunings where strong energy deviations occurs but at very small  $k$ -range at some finite  $k$ . Hence, it cannot replicate the two-peaked inverted dispersion, which forms a ring in  $k$ -space, presented in the main text. Secondly, at positive detuning, the

exciton-like branch is constrained below the bare exciton line (due to level repulsion) and will only approach the exciton line by increasing in energy at large  $k$ . This cannot replicate the experimental results where the lower branch decreases in energy at higher  $k$ , as it approaches the exciton line.

## S5: CHARACTERIZATION OF MONOLAYER-INTEGRATED MICROCAVITIES AND THE OPTICAL PROPERTIES OF MONOLAYER WS<sub>2</sub> ON DBR SUBSTRATES

The structure investigated in the main text was fabricated with the method presented in [8]. In contrast to this work, we deposited the DBR substrate consisting of 17.5 SiN<sub>x</sub>/SiO<sub>x</sub> layers on top of a silicon chip via plasma-enhanced chemical vapour deposition (PECVD) at 300 °C, and finalised it with 100 nm of SiO<sub>2</sub>, of which 80 nm was grown via sputtering and 20 nm via atomic layer deposition (ALD). The WS<sub>2</sub> monolayer was then mechanically exfoliated [9] from bulk WS<sub>2</sub> sourced from HQ graphene [10] and placed onto the DBR substrate. As a reference, we placed a WS<sub>2</sub> monolayer onto a high-quality SiO<sub>2</sub> chip from Nova Materials [11].

After spin-coating the 80 nm thick PMMA cavity spacer and protective layer on both samples, we compare the effects of the substrate on the exciton–photon interactions in these monolayer by measuring the reflectivity spectra with a tungsten halogen white light source.

Fig. S5a presents the reflectivity contrast spectra  $\Delta R/R_{Ref}$  of both samples. The spectra were calculated by measuring the reflectivity spectra on the monolayer  $R$  and next to the monolayers  $R_{Ref}$ , with  $\Delta R = R - R_{Ref}$ . When fitting a Voigt-profile to the high-energy shoulder of the reflectivity spectrum of the monolayer placed on the DBR chip, we find for the exciton energy and linewidth  $E_X \approx 2.007$  eV and  $\gamma_x \approx 63$  meV, respectively.

Here, the product of amplitude and linewidth at the exciton energy scales with the exciton oscillator strength quantifying the exciton–photon interactions [12]. Clearly, the oscillator strength of the monolayer on the DBR chip is significantly lower compared to that of the reference sample. Therefore, the DBR substrate lowers the exciton oscillator strength of the monolayer compared to that when placed onto a high quality substrate, which is possibly due to environmental charge doping, dielectric disorder and strain [13–18].

Moreover, as we have demonstrated in [8], the exciton oscillator strength will further decrease after deposition of the top structure, consisting of the SiO<sub>x</sub> spacer and the top DBR, via PECVD at 150 °C. While a reduction of the exciton oscillator strength is normally avoided for polariton research, it amplifies the effects of dissipative coupling on the polariton dispersion and allows us in this work to observe the negative mass of the lower polariton branch.

After finalising the microcavity, we further measured the reflectivity spectrum outside of the monolayer area at zero momentum  $k = 0$  to characterise the photon mode. Fig. S5b

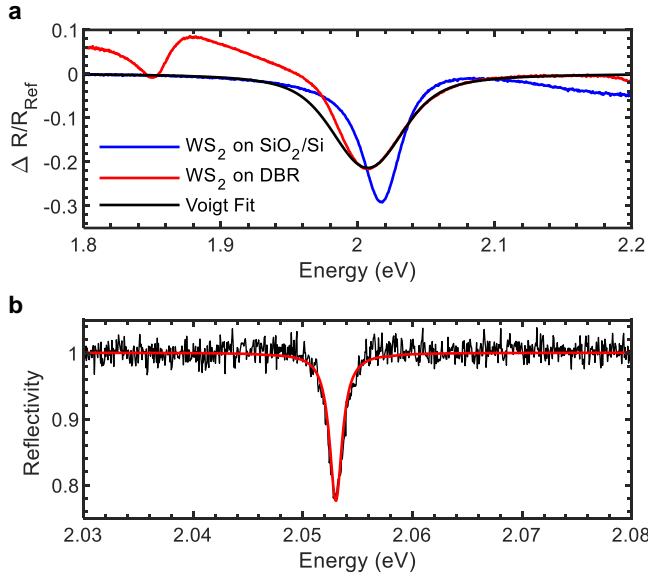


FIG. S5. **Characterisation of the microcavity discussed in the main text and the excitonic response of monolayer WS<sub>2</sub> on the DBR substrate.** (a) The derivative of the reflectivity contrast spectrum of a WS<sub>2</sub> monolayer capped with PMMA on (blue) a high-quality SiO<sub>2</sub> substrate and (red) on the DBR chip. The reflectivity contrast spectrum was fitted with (black) a Voigt profile. (b) Reflectivity spectrum of the microcavity next to the monolayer region.

shows a strong reflectivity dip at  $E \approx 2.053$  meV marking the cavity resonance  $E_c$ , which is positively detuned from the bare exciton energy. The linewidth of the cavity mode is  $\gamma_c = 1.4$  meV and therefore, the microcavity has a Q-factor of around 1500.

\* [matthias.wurdack@anu.edu.au](mailto:matthias.wurdack@anu.edu.au)

† [elena.ostrovskaya@anu.edu.au](mailto:elena.ostrovskaya@anu.edu.au)

‡ [eliezer.estrecho@anu.edu.au](mailto:eliezer.estrecho@anu.edu.au)

- [1] A. Kormányos, G. Burkard, M. Gmitra, J. Fabian, V. Zolyomi, N. D. Drummond, and V. Falko, *k p* theory for two-dimensional transition metal dichalcogenide semiconductors, *2D Materials* **2**, 022001 (2015).
- [2] X. Li, J. T. Mullen, Z. Jin, K. M. Borysenko, M. Buongiorno Nardelli, and K. W. Kim, Intrinsic electrical transport properties of monolayer silicene and MoS<sub>2</sub> from first principles, *Phys. Rev. B* **87**, 115418 (2013).
- [3] Z. Jin, X. Li, J. T. Mullen, and K. W. Kim, Intrinsic transport properties of electrons and holes in monolayer transition-metal dichalcogenides, *Phys. Rev. B* **90**, 045422 (2014).
- [4] M. Selig, D. Christiansen, M. Katzer, M. V. Ballottin, P. C. M. Christianen, and A. Knorr, Impact of optically pumped non-equilibrium steady states on luminescence emission

of atomically-thin semiconductor excitons, *arXiv:2201.03362* (2022).

- [5] D. Xiao, G.-B. Liu, W. Feng, X. Xu, and W. Yao, Coupled spin and valley physics in monolayers of mos<sub>2</sub> and other group-vi dichalcogenides, *Phys. Rev. Lett.* **108**, 196802 (2012).
- [6] M. Selig, F. Katsch, R. Schmidt, S. M. de Vasconcellos, R. Bratschitsch, E. Malic, and A. Knorr, Ultrafast dynamics in monolayer transition metal dichalcogenides: Interplay of dark excitons, phonons, and intervalley exchange, *Physical Review Research* **1**, 022007 (2019).
- [7] A. Thränhardt, S. Kückenburg, A. Knorr, T. Meier, and S. W. Koch, Quantum theory of phonon-assisted exciton formation and luminescence in semiconductor quantum wells, *Phys. Rev. B* **62**, 2706 (2000).
- [8] T. Yun, E. Estrecho, A. G. Truscott, E. A. Ostrovskaya, and M. J. Wurdack, Fabrication of high-quality pmma/sio<sub>2</sub> spaced planar microcavities for strong coupling of light with monolayer ws<sub>2</sub> excitons, *arXiv:2204.01181* (2022).
- [9] K. S. Novoselov, A. K. Geim, S. V. Morozov, D. Jiang, Y. Zhang, S. V. Dubonos, I. V. Grigorieva, and A. A. Firsov, Electric field effect in atomically thin carbon films, *Science* **306**, 666 (2004), <https://www.science.org/doi/pdf/10.1126/science.1102896>.
- [10] <http://www.hqgraphene.com>.
- [11] <http://www.nowafab.com>.
- [12] N. Lundt, A. Maryński, E. Cherotchenko, A. Pant, X. Fan, S. Tongay, G. Sek, A. V. Kavokin, S. Höfling, and C. Schneider, Monolayered MoSe<sub>2</sub>: a candidate for room temperature polaritonics, *2D Materials* **4**, 015006 (2016).
- [13] Y. Yu, Y. Yu, C. Xu, Y.-Q. Cai, L. Su, Y. Zhang, Y.-W. Zhang, K. Gundogdu, and L. Cao, Engineering substrate interactions for high luminescence efficiency of transition-metal dichalcogenide monolayers, *Advanced Functional Materials* **26**, 4733 (2016), <https://onlinelibrary.wiley.com/doi/pdf/10.1002/adfm.201600418>.
- [14] S. Lippert, L. M. Schneider, D. Renaud, K. N. Kang, O. Ajayi, J. Kuhnert, M.-U. Halbach, O. M. Abdulmunem, X. Lin, K. Hassoon, S. Edalati-Boostan, Y. D. Kim, W. Heimbrod, E.-H. Yang, J. C. Hone, and A. Rahimi-Iman, Influence of the substrate material on the optical properties of tungsten diselenide monolayers, *2D Materials* **4**, 025045 (2017).
- [15] A. Raja, L. Waldecker, J. Zipfel, Y. Cho, S. Brem, J. D. Ziegler, M. Kulig, T. Taniguchi, K. Watanabe, E. Malic, T. F. Heinz, T. C. Berkelbach, and A. Chernikov, Dielectric disorder in two-dimensional materials, *Nature Nanotechnology* **14**, 832 (2019).
- [16] Z. Khatibi, M. Feierabend, M. Selig, S. Brem, C. Linderäl, P. Erhart, and E. Malic, Impact of strain on the excitonic linewidth in transition metal dichalcogenides, *2D Materials* **6**, 015015 (2018).
- [17] K. He, C. Poole, K. F. Mak, and J. Shan, Experimental demonstration of continuous electronic structure tuning via strain in atomically thin MoS<sub>2</sub>, *Nano Letters* **13**, 2931 (2013), pMID: 23675872, <https://doi.org/10.1021/nl4013166>.
- [18] J. Martín-Sánchez, A. Mariscal, M. D. Luca, A. T. Martín-Luengo, G. Gramse, A. Halilovic, R. Serna, A. Bonanni, I. Zardo, R. Trotta, and A. Rastelli, Effects of dielectric stoichiometry on the photoluminescence properties of encapsulated WSe<sub>2</sub> monolayers, *Nano Research* **11**, 1399 (2018).